Contents list available at CBIORE journal website

International Journal of Renewable Energy Development

Journal homepage: https://ijred.cbiore.id

Research Article

Experimental and DFT investigation of $LiFePO_4$/graphene composites prepared via shear exfoliation route

Amun Amri[a*], Mawaddah[a], Alfatlian[a], Sunarno[a], Fri Murdiya[b], Mazhibayev Assylzhan[c], Khairulazhar Jumbri[d], Mohammednoor Altarawneh[e], Chun-Chen Yang[f], Sulistyo Saputro[g], M. Mahbubur Rahman[h]

[a]*Department of Chemical Engineering, University of Riau, Pekanbaru, 28293, Indonesia*

[b]*Department of Electrical Engineering, University of Riau, Pekanbaru, 28293, Indonesia*

[c]*Department of Chemistry, Dulaty University, Taraz, 080000, Kazakhstan*

[d]*Department of Fundamental and Applied Sciences, Universiti Teknologi PETRONAS, Seri Iskandar, 32610, Malaysia*

[e]*Department of Chemical and Petroleum Engineering, United Arab Emirates University, 15551, United Arab Emirates*

[f]*Battery Research Center of Green Energy, Ming Chi University of Technology, Taishan, New Taipei City, 24301, Taiwan*

[g]*Department of Natural Science Education, Universitas Sebelas Maret, Surakarta, 57126, Indonesia*

[h]*Deparment of Physics, Jahangirnagar University, Savar, Dhaka, 1342, Bangladesh*

Abstract. The performance of $LiFePO_4$ (LFP) cathodes was successfully enhanced by incorporating two types of graphene obtained through green and low-cost liquid shear exfoliation processes. Commercial LFP was combined with few-layer graphene (FLG) and very few-layer graphene (VFLG), with compositions ranging from 0-4 wt.%. LFP, LFP/FLG, and LFP/VFLG, were characterized using electrochemical impedance spectroscopy (EIS), charge–discharge (CD), XRD, FTIR, and FESEM–EDX. Density functional theory (DFT) calculations were further employed to probe the electronic structure of LFP and an idealized LFP(001)/pristine-graphene interface as a baseline model for interfacial electronic coupling. DFT indicated interfacial charge redistribution and the emergence of C-2p π-derived states near the Fermi level, resulting in bandgap narrowing relative to pristine LFP and suggesting an additional electronic percolation pathway at the interface. Experimentally, EIS showed that VFLG reduced charge-transfer resistance and increased effective electrochemical conductivity, while FLG addition was associated with improved interfacial charge-transfer behavior inferred from EIS. CD tests at 0.5 C showed that the 4 wt.% FLG and 4 wt.% VFLG electrodes delivered the highest specific capacities of 29.98 mAh/g and 44.66 mAh/g, corresponding to increases of 81.9% and 170.5% compared to bare LFP. XRD and FTIR confirmed that LFP phase integrity was maintained, and FESEM–EDX revealed a uniform particle distribution with well-dispersed graphene networks. Overall, these results demonstrated that shear-exfoliated graphene effectively improved electronic connectivity and charge-transfer behavior in LFP cathodes, supported by consistent electrochemical measurements and electronic-structure insights from DFT.

Keywords: $LiFePO_4$ (LFP) cathode, Graphene composite, Electrochemical performances, DFT

Received: 12th Oct 2025, Revised: 6th Dec 2025, Accepted: 28th Dec 2025, Available online: 18th January 2026

1. Introduction

Lithium-ion batteries employing lithium iron phosphate ($LiFePO_4$/LFP) cathodes have attracted sustained interest owing to their high round-trip efficiency, long cycle life, thermal safety, and a theoretical capacity of 170 mAh/g (Chen *et al.,* 2020, Hassan & Al-Timimi, 2025, Zhang *et al.*, 2012). In addition, LFP is environmentally benign and cost-effective compared with layered oxide cathodes (Zhang *et al.*, 2012). Nevertheless, the practical performance of LFP is often limited by its intrinsically poor electronic conductivity and modest lithium-ion diffusivity, which together increase polarization and hinder full usage of the active material (Li *et al.,* 2019, Mohanty *et al.,* 2023).

To address these limitations, extensive strategies have been explored, including carbon coating, conductive additives, morphology/size control, and heteroatom doping (Eftekhari, 2017, Stenina *et al.*, 2022). Among them, graphene has emerged as a particularly promising conductive network due to its large specific surface area, high carrier mobility, and mechanical robustness that together promote fast electron percolation and stable interfaces inside composite electrodes (Hu *et al.,* 2013, Imteyaz & Rafiuddin, 2023). Prior studies reported capacity improvements and reduced polarization when graphene is introduced into LFP electrodes by various routes, electrochemical exfoliation, spray-drying/carbon-coating, CVD/foam scaffolds, or chemical reduction of graphite oxide, though some of these methods involve costly or less

* Corresponding author
Email: amun.amri@eng.unri.ac.id (A.Amri)

https://doi.org/10.61435/ijred.2026.61976
ISSN: 2252-4940/© 2026.The Author(s). Published by CBIORE

environmentally friendly chemistries and may compromise tap density (Ding *et al.,* 2019, Fu *et al.,* 2019, Guan *et al.,* 2017, Hu *et al.,* 2013, Ma *et al.,* 2018).

Building on this context, low-cost liquid shear exfoliation provides an attractive pathway to produce few-layer graphene (FLG) and very-few-layer graphene (VFLG) at scale with benign solvents and simple hardware (Amri *et al.,* 2021, Varrla *et al.,* 2014). In our previous work, we integrated VFLG into LFP precursors via a sol-gel route and observed improved structural–electrochemical responses, albeit with a cumbersome synthesis chain (Amri *et al.,* 2024). The present study simplifies the manufacturing route by directly blending commercial LFP with FLG (from TASE) and VFLG (from TSSE) at low loadings (0–4 wt.%), followed by conventional electrode fabrication. This approach shortens the supply chain while preserving the advantages of graphene conductive networks.

Despite substantial experimental evidence that graphene can enhance LFP performance, the microscopic interfacial electronic mechanism at the LFP/graphene (LFP/G) contact remains insufficiently clarified. Many reports emphasize electrochemical metrics, dispersion quality, or morphological factors, whereas the interfacial electronic structure, particularly density-of-states (DOS) features near the Fermi level, band alignment, and the implications for charge-transfer resistance, has been less systematically correlated with electrochemical observations (Rossouw *et al.,* 2017, H. Wang *et al*., 2016), In these studies, the LFP/G interface was modeled, but the calculated electronic features were not directly linked to experimental impedance or charge–discharge responses. This gap is critical because polarization and electrochemical overpotential in LFP are strongly influenced by electron availability during the Fe^{2+}/Fe^{3+} redox process and by interfacial charge-transfer efficiency during Li^{+} (de)intercalation. To address this gap from an electronic-structure perspective, we combine experimental characterization with first-principles calculations. In this work, the DFT interface is intentionally formulated as an idealized baseline to isolate interfacial electronic coupling. The potential implications of defects and/or limited functional groups in shear-exfoliated graphene are discussed when interpreting the calculated trends.

This paper reports the preparation and characterization of LFP/FLG and LFP/VFLG composites (0–4 wt.%), evaluates their electrochemical behavior (EIS and CD at 0.5 C), examines structural/chemical integrity (XRD, FTIR, FESEM–EDX), and elucidates the electronic origin of performance gains via DFT-based DOS analysis of an LFP(001)/G interface using spin-polarized calculations in CASTEP with the LDA–PWC functional (Perdew & Wang, 1992, Segall *et al*., 2002). The results show that adding 4 wt.% FLG and 4 wt.% VFLG yields the highest discharge capacities of 29.98 mAh/g and 44.66 mAh/g at 0.5 C, corresponding to increases of 81.9% and 170.5% relative to bare LFP. The DFT results indicate interfacial electronic coupling that introduces graphene-derived states near the Fermi level and narrows the effective bandgap, providing an atomistic rationale consistent with the experimentally observed reduction in charge-transfer resistance. The novelty of this work lies in the integration of low-cost, shear-exfoliated FLG and VFLG with commercial LFP through a simple blending route compatible with practical electrode manufacturing, together with a direct correlation between the observed electrochemical improvements and baseline electronic-structure insights that clarify graphene's role in enhancing interfacial electronic connectivity rather than acting solely as a passive conductive additive.

2. Experimental

2.1 Preparation of $LiFePO_4$/graphene (LFP/G)

Low-cost graphene (FLG and VFLG) was derived from graphite via straightforward and environmentally friendly methods, namely turbulence-assisted shear exfoliation (TASE) (Varrla *et al.,* 2014) and a two-step shear exfoliation process (Amri *et al.,* 2021), respectively. In this study, graphene quality metrics such as flake thickness (layer number), lateral size distribution, and Raman defect indicators were not re-measured for the current batch. Instead, because the TASE/TSSE procedures and operating conditions followed the same validated protocol, we referred to our previous characterization (Amri *et al.,* 2021). In that work, TSSE-derived VFLG was validated by Raman and TEM–HRTEM to be predominantly 1–2 layers with a mean lateral size of ~375 nm and a low defect ratio ($I_D/I_G \approx 0.146$), whereas TASE-derived FLG exhibited a thicker few-layer structure (~4 layers) with a smaller mean lateral size of ~187 nm and a higher defect ratio ($I_D/I_G \approx 0.536$). These I_D/I_G values indicated that TSSE produced graphene with substantially lower shear-induced disorder/edge-related defects than TASE under the validated conditions. Accordingly, the Raman-based defect trend supported the use of VFLG as a higher-quality conductive additive, while FLG was expected to contain more edge/defect sites due to its smaller flake size. These values were therefore provided as reference characteristics for graphene produced by the same protocol, while the present work focused on the electrochemical behavior of the resulting LFP/G composites.

The materials used in this study included commercial LFP with 99.9% purity, obtained from Xiamen Tob New Energy Technology (China) and used as received. The LFP/G composite was synthesized by mixing commercial LFP with FLG and VFLG at concentrations of 0-4 wt.%. The mixture was then thoroughly stirred to produce a homogeneous black paste. The LFP/G paste was dried in an oven at 60°C for 24 hours. The dried paste was then processed following the procedure for fabricating 18650-type cylindrical cell batteries (Hasanah *et al.,* 2020).

2.2 Characterization

The electrochemical characteristics of commercial LFP and LFP/G as lithium-ion battery cathodes were investigated using charge-discharge (CD) analysis and electrochemical impedance spectroscopy (EIS). The EIS was performed using an LCR meter (0.5-10^4 Hz). CD tests were conducted with a NEWARE Battery Analyzer and BTS software at a 2–3.8 V voltage range for 20 cycles. Additionally, commercial LFP and LFP/G composites were subjected to a series of analyses, including X-ray diffraction (XRD), Fourier transform infrared spectroscopy (FTIR), and field emission scanning electron microscopy with energy dispersive X-ray (FESEM-EDX), to ascertain their characteristics. The XRD analysis was conducted employing a SHIMADZU XRD-7000 X-ray diffractometer with a Cu Kα source, a wavelength (λ) of 1.5406 Å, and a diffraction angle (2θ) range of 10°–80°. The resulting XRD data were analyzed using HighscorePlus, OriginPro, and VESTA software to obtain diffractograms and crystallographic structures. FTIR measurements were conducted with a Perkin-Elmer UATR Spectrum Two in the 4000–400 cm^{-1} wavenumber range. FESEM-EDS was performed using a Thermo Scientific Quattro S FESEM equipped with an EDS detector. The FESEM-EDS data were analyzed using ESPRIT Compact software to examine the composition and distribution of elements in the LFP and LFP/G samples.

2.3 Computational method (DFT calculations)

To complement the experimental findings, first-principles density functional theory (DFT) calculations were performed using the CASTEP code (Segall *et al*., 2002). The local density approximation (LDA–PWC) (Perdew & Wang, 1992) functional was employed with a plane-wave cutoff energy of 400 eV and a 3 × 2 × 1 κ-points sampling. Spin-polarized calculations were carried out to describe the Fe^{2+}/Fe^{3+} electronic configuration in LFP. A (001) surface slab of orthorhombic LFP (space group *Pnma*) was constructed to represent the preferred lithium-ion diffusion plane. For the LFP/G model, a graphene basal plane was represented by a single pristine graphene monolayer placed above the LFP surface, and a vacuum spacing of 15 Å was applied to avoid spurious interlayer interactions. Atomic positions were relaxed until the forces were below 0.01 eV/Å. The interaction between LFP and graphene was analyzed in terms of optimized interfacial distance, charge transfer, and density of states (DOS) distribution. It was noted that the present interface model was an idealized first-order approximation that isolated the electronic coupling between the LFP surface and an sp^2 carbon π-network. In practical high-shear exfoliation, graphene flakes could exhibit edge-related defects (e.g., vacancies, wrinkles, and grain boundaries) and, depending on processing history and stabilizer/solvent environment, a finite amount of oxygen-containing functional groups. These realistic features were not explicitly included in the current atomistic model. Therefore, the DFT results in this work were interpreted primarily to capture qualitative electronic trends and baseline interfacial band alignment, while the absolute magnitude of charge transfer or bandgap modification could differ for defect- or functionalized graphene.

3. Results and discussion

3.1 Electrochemical impedance spectroscopy (EIS) analysis

Fig. 1 shows the EIS results for commercial LFP and LFP by the addition of 1–4 wt.% few-layer graphene (LFP/FLG). Each LFP/FLG sample in Fig. 1 displays a plot that does not form a semi-circle pattern. According to Mahesh *et al.* (2012), the absence of a semi-circle pattern in the samples is due to the high-frequency region, where the diffusion path becomes short,

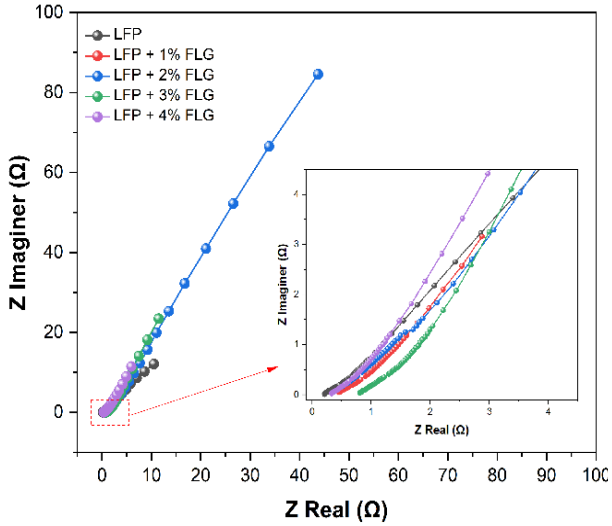

Fig. 1 Electrochemical impedance spectroscopy (EIS) results for commercial LFP and LFP/FLG samples with 1-4 wt.% FLG addition using 18650-type cylindrical batteries.

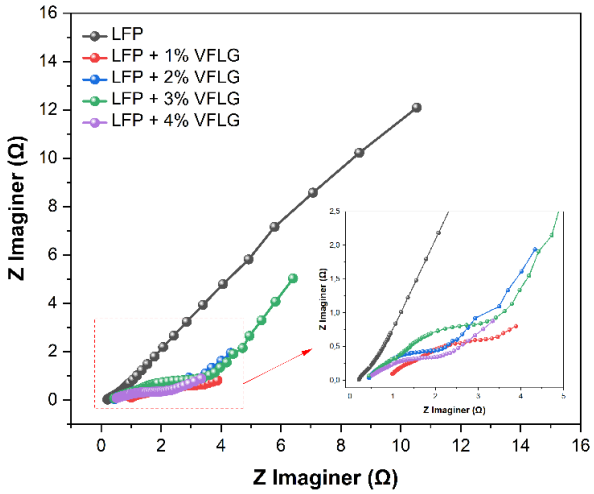

Fig. 2 Electrochemical impedance spectroscopy (EIS) results for commercial LFP and LFP /VFLG samples with 1-4 wt.% VFLG addition using 18650-type cylindrical batteries.

or the small resistance provided by the interface area between the electrolyte and the electrode material for lithium-ion migration, allowing lithium ions to diffuse without significant hindrance (Mahesh *et al.,* 2012). However, the LFP/FLG samples show a straight line with an angle greater than 45°, indicating the Warburg diffusion coefficient and its relation to lithium-ion diffusion at the electrode (Liu *et al*., 2017).

Fig. 1 shows that sample 4 wt.% FLG exhibits a steeper and higher slope than samples 0-3 wt.% FLG. The increased FLG in LFP accelerates ion diffusion within the electrode, improving electrode performance. During intercalation, ions or molecules are reversibly inserted into the empty sites in the crystal lattice. Although its relatively small capacity, intercalation minimizes volume changes and mechanical stresses during alkali ions' repeated insertion and extraction (Massé *et al*., 2017). The slope of the LFP/FLG line is greater than that of LFP without graphene addition, indicating that the lithium-ion diffusion in LFP/FLG occurs more rapidly. This finding is consistent with Shang *et al.* (2014), who reported that graphene can improve the diffusion coefficient of lithium ions and the intercalation and deintercalation kinetics of lithium (Shang *et al.,* 2014).

The EIS results for LFP samples with the addition of very few-layer graphene (LFP/VFLG) are shown in Fig. 2. In Fig. 2, samples 1-4 wt.% VFLG form a semi-circle pattern and a straight line. The sample LFP without graphene addition shows a linear response without the semi-circle feature, as illustrated in Fig. 2. According to Jayasree *et al.* (2020), an electrode sample that only shows a linear response without a semi-circle feature indicates capacitive charge storage with poor electronic conductivity (Jayasree *et al.,* 2020). In Fig. 2, the LFP/VFLG samples display curves with a semi-circular pattern associated with the charge transfer resistance (R_{ct}) process. Charge-transfer resistance (R_{ct}) is the resistance encountered during the electrochemical reaction at the interface between the electrolyte solution and the electrode. This resistance corresponds to the barrier that electrons must pass through at the electrode surface to interact with adsorbed species or vice versa. R_{ct} is related to the electrode potential, where an increase in voltage leads to a decrease in resistance (Wang *et al.,* 2021). The value of R_{ct} for each sample is obtained from the diameter of the semi-circle formed in the EIS results. A significant R_{ct} value indicates low reaction rate of Li^+ at the LFP/electrolyte interface (Fathollahi *et al.*, 2015). The calculated R_{ct} values for the LFP/VFLG composites are presented in Table 1.

Table 1
Resistive resistance values for LFP/VFLG cathode

Sample	R_t (Ω)	R_e (Ω)	R_{ct} (Ω)
LFP + 1 wt.% VFLG	3.05	0.99	2.06
LFP + 2 wt.% VFLG	2.23	0.45	1.78
LFP + 3 wt.% VFLG	3.21	0.44	2.78
LFP + 4 wt.% VFLG	2.05	0.52	1.53

Table 1 displays the resistance values for the LFP/VFLG samples, where R_t represents the total resistance and R_e represents the electrolyte resistance. As shown in Table 1, the R_{ct} values for each LFP/VFLG sample decrease after the addition of VFLG. The reduction in R_{ct} suggests improved charge transfer capacity and double-layer capacitance at the electrode-electrolyte interface (Fathollahi *et al.,* 2015). Sample 4 wt.% VFLG exhibited the smallest semi-circle diameter, indicating a low impedance value and suggesting better lithium-ion diffusion. The graphene network significantly aids the fast transport of Li ions, and the reduced impedance at the solid-electrolyte interface is ascribed to the incorporation of graphene layers in the LFP/VFLG (Li *et al*., 2014). This is consistent with the study by Guan *et al.* (2019), which reported that an increased graphene content leads to lower resistance, better rate performance, and improved overall conductivity (Guan *et al.,* 2019). However, in sample 3 wt.% VFLG, the semi-circle pattern exhibits the largest diameter, indicating higher impedance and slower lithium-ion diffusion. Wang *et al.* (2016) reported that graphene tends to aggregate due to its unstable dispersion. Therefore, surfactants are added during the TASE or TSSE methods as dispersion agents (Varrla *et al.,* 2014, Wang *et al.,* 2016). Although surfactants can help disperse graphene and prevent aggregation, several factors can influence the formation of aggregates in the LFP/G active material. One such factor is the large specific surface area of graphene, which makes it difficult to homogeneously disperse in the composite without disrupting the size of the graphene sheets (Gao et al., 2008). According to Gu and Hu (2021), the addition of a large amount of graphene leads to dispersion difficulties. It may cause aggregation, resulting in incomplete conductive network formation and voids in the layer, which can hinder electrical conductivity and reduce the number of conductivity paths formed (Gu & Hu, 2021).

EIS was used to evaluate interfacial kinetics and the apparent lithium-ion diffusion coefficient in the cathode. Table 2 shows the Warburg coefficient (σ) extracted from the low-frequency EIS diffusion tail (linear Z′ vs. $\omega^{-1/2}$, where $\omega = 2\pi f$) and the corresponding apparent/chemical lithium-ion diffusion coefficient D_{Li}^+, which was calculated using Equation (1). In impedance theory, the semi-infinite Warburg response yields a linear dependence of Z′ vs. $\omega^{-1/2}$, so σ is directly extracted as the slope of the Warburg plot (L. Wang *et al*., 2012, Zhang *et al.,* 2024).

$$\boldsymbol{D_{Li^+}} = \frac{\boldsymbol{R^2T^2}}{\boldsymbol{2A^2n^4F^4C^2\sigma^2}} \quad (1)$$

Where n = 1 for Li^+, and T = 298 °K, R (8.314 J/mol K) and F (96485 C/mol) are the gas and Faraday constants. The Li concentration in fully lithiated LFP was approximated as $C = \rho/M \approx 3.60/157.76 \approx 2.28\times10^{-2}$ mol/cm^3 (one Li per formula unit), and the geometric electrode area was A = 26.5 × 5.6 = 148.4 cm^2. Because diffusion in two-phase insertion materials is spatially and temporally non-uniform, the extracted D_{Li+} should be interpreted as an apparent/effective value mainly intended for comparative analysis among samples (Rui *et al*., 2011).

Table 2
Warburg coefficient (σ) and apparent Li^+ diffusion coefficient D_{Li+} estimated from EIS

Sample (wt.%)	Warburg fit window (Hz)	σ (Ωs$^{-1/2}$)	R^2	D_{Li}^+ (cm^2/s)
LFP	1.87 – 18.3	3.55	0.99	2.46 x 10^{-16}
LFP+1% FLG	1.90 – 8.76	5.61	0.99	9.81 x 10^{-17}
LFP+2% FLG	0.70 – 6.60	7.34	0.99	5.74 x 10^{-17}
LFP+3% FLG	1.36 – 18.3	5.80	0.99	9.18 x 10^{-17}
LFP+4% FLG	3.61 – 31.92	5.10	0.99	1.18 x 10^{-16}
LFP+1% VFLG	22.03 – 50.74	6.82	0.99	6.65 x 10^{-17}
LFP+2% VFLG	13.86 – 31.92	5.24	0.99	1.13 x 10^{-16}
LFP+3% VFLG	6.02 – 13.86	5.98	0.99	8.65 x 10^{-17}
LFP+4% VFLG	0.01 – 0.19	0.37	0.99	2.27 x 10^{-14}

Based on Table 2, pristine LFP exhibits D_{Li+} on the order of 10^{-16} cm^2/ s, while most FLG-containing electrodes remain within ~10^{-17}–10^{-16} cm^2/s, indicating only modest changes in the diffusion-related impedance under the present conditions. In contrast, the 4 wt.% VFLG composite shows a much smaller σ and therefore a markedly higher apparent D_{Li+} (~10^{-14} cm^2/ s), consistent with substantially reduced diffusion polarization (because even a moderate reduction in σ produces a large increase in D via Equation (1)) (Zhao *et al*., 2025). Such enhancement is plausibly attributed to a more effective conductive/interfacial network enabled by VFLG (e.g., improved percolation and interfacial pathways), which can reduce polarization and facilitate coupled charge/ion transport in composite electrodes, an interpretation that is also consistent with the lower interfacial resistance trends discussed from EIS fitting (Cruz-Manzo & Greenwood, 2020). It should be emphasized that the extracted D_{Li+} values represent apparent/chemical diffusion coefficients derived from porous composite electrodes and therefore depend on model assumptions (e.g., semi-infinite diffusion in the selected low-frequency window and the use of geometric area). Consequently, these values are best interpreted as comparative indicators of Li^+ transport trends among samples measured under identical conditions, rather than absolute intrinsic diffusivities (Barsoukov & Macdonald, 2005).

3.2 Charge-discharge (CD) analysis

Fig. 3 shows the polarization curve obtained from the CD analysis of an 18650-type cylindrical battery with commercial LFP cathode material at a rate of 0.5 C, conducted up to the 20th cycle. The CD test assessed the battery's ability to handle the current load. The capacity obtained for the sample during the first charge cycle was 80.66 mAh, while the discharge capacity for the sample was 64.4 mAh. By the 20th cycle, the charge capacity had decreased to 45.90 mAh, and the discharge capacity was 44.87 mAh. The amount of LFP used in the CD test was 3.9 grams. The specific capacity of the battery after the first cycle was calculated to be 16.51 mAh/g, and after the 20th cycle, it was 11.51 mAh/g. The obtained results are lower than the theoretical specific capacity of LFP, which should reflect the complete intercalation of lithium ions. This decrease may be attributed to several factors, such as imperfect cycling, material defects, and internal resistance that hinder the movement of Li^+ ions, thereby reducing their practical specific capacity (Bellache *et al*., 2018, Wang, 2011). Therefore, we also conducted tests on the LFP precursor to compare and examine the consequence of graphene addition on the LFP cathode. The reactions occurring

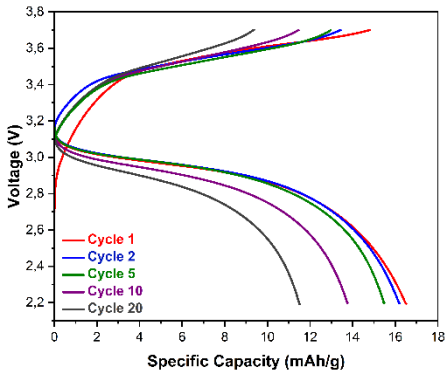

Fig. 3 Charge/discharge curves for commercial LFP sample.

throughout the charging and discharging cycles are shown in Equations (2–4) (Dixit, 2019).

$$LiFePO_4 \leftrightarrow Li_{1-x}FePO_4 + xLi^+ + xe \quad \textbf{(positive electrode side)} \quad (2)$$

$$C + xLi^+ + xe \leftrightarrow Li_xC \quad \textbf{(negative electrode side} \quad (3)$$

$$LiFePO_4 + C \leftrightarrow Li_{1-x}FePO_4 + Li_xC \quad \textbf{(overall reaction)} \quad (4)$$

Fig. 4 shows the charge-discharge curve for LFP with the addition of 1 wt.% FLG and VFLG at the same current rate over 20 cycles. Fig. 4(a) presents the CD test at a rate of 0.5 C for the LFP/FLG (1 wt.% FLG) sample, which only completed one cycle, resulting in a single polarization curve. In the first cycle, the LFP/FLG sample revealed a discharge capacity of 130.48 mAh and a charge capacity of 178.57 mAh. The charge/discharge curves for the 1st, 2nd, 5th, 10th, and 20th cycles of the LFP cathode with 1 wt.% VFLG addition are shown and compared in Fig. 4(b). In the first cycle, the discharge capacity was 90.38 mAh and the charge capacity was 150.82 mAh. By the 20th cycle, charge and discharge capacities decreased to 76.05 mAh and 76.18 mAh, respectively. The weight of the LFP/VFLG used in the CD test was 2.3 grams, so the specific capacity was determined to be 39.29 mAh/g after the first cycle and 33.12 mAh/g after the 20th cycle. The decrease in specific capacity with the increasing number of cycles has been previously reported by (Li *et al.,* 2018).

Fig. 5 shows the charge/discharge curves for LFP with the addition of 4 wt.% FLG and VFLG at the same current rate over 20 cycles. It can be observed that there is a redox reaction for the Fe^{+3}/Fe^{+2} pair during the lithium deintercalation and intercalation processes in the sample, indicated by a slight flat region in the voltage range of 3.0 – 3.1 V, as shown by equation (1) (Amri et al., 2024). Furthermore, the charge/discharge curve for LFP/VFLG is smoother compared to that of LFP/FLG. This indicates an improvement in electrochemical kinetics, allowing for more efficient energy utilization in LFP/VFLG (Amri *et al.,* 2024).

Figs. 3-5 show the discharge curves with a flat discharge profile, representing the effect of minimal changes in the reactant and product materials until the active material is nearly depleted. From Figs. 3-5, it is evident that the battery capacity decreases with increasing cycles. One of the causes is that when lithium ions first migrate from the cathode to the anode and are stored at the electrolyte-anode interface, they do not fully return during usage. These trapped lithium ions form a new structure known as the solid electrolyte interphase (SEI) (Gan et al., 2013). A comparison of the specific capacities for each sample is presented in Table 3.

As shown in Table 3, in the first cycle, the LFP precursor exhibits a discharge-specific capacity of approximately ~16.51 mAh/g. In contrast, LFP/FLG and LFP/VFLG show significantly increased discharge specific capacities of 29.98 mAh/g and 44.66 mAh/g, corresponding to increases of 81.9% and 170.5%, respectively, compared to bare LFP. These results confirm that the incorporation of graphene effectively enhances the discharge-specific capacity and significantly benefits the

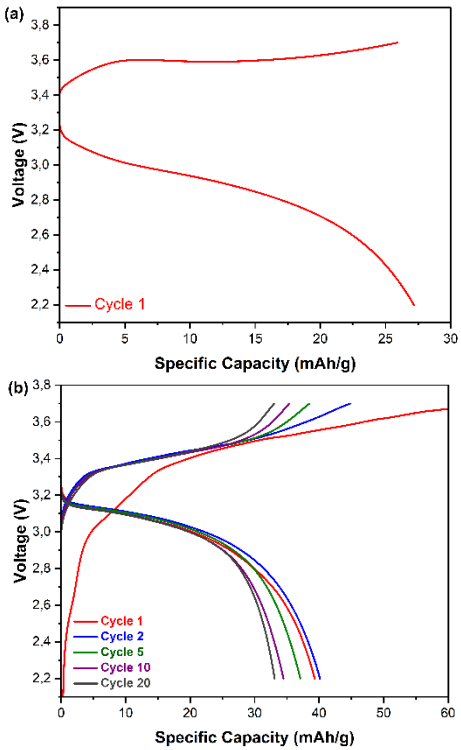

Fig. 4 Charge/discharge curves for the sample with 1 wt.% graphene addition: (a) LFP/FLG, (b) LFP/VFLG.

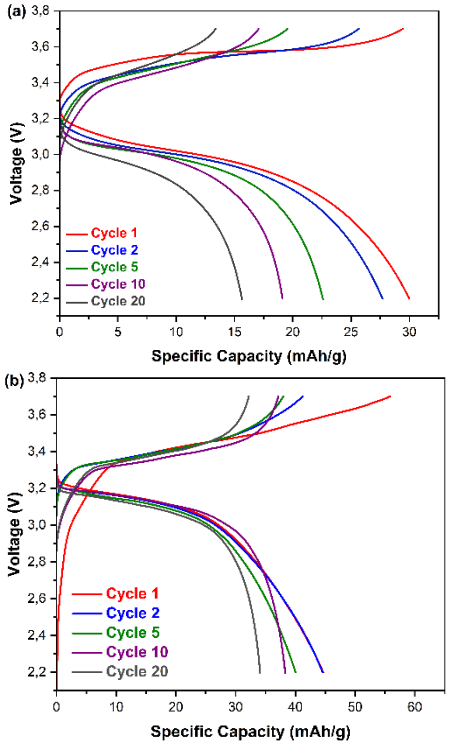

Fig. 5 Charge/discharge curves for the sample with 4 wt.% graphene addition: (a) LFP/FLG, (b) LFP/VFLG.

Table 3
Specific capacity in the first cycle for LFP/G cathodes.

Sample	Discharge Capacity (mAh)	LFP Weight (grams)	Specific Capacity (mAh/g)
LFP	64.40	3.90	16.51
LFP + 1 wt.% FLG	130.48	4.80	27.18
LFP + 1 wt.% VFLG	90.38	2.30	39.29
LFP + 4 wt.% FLG	164.91	5.50	29.98
LFP + 4 wt.% VFLG	87.09	1.95	44.66

LFP cathode. The low specific capacity of LFP can be attributed to factors such as higher irregularity levels, poor cell parameters, smaller specific surface area, lower crystallinity and morphology, and larger particle size (Amri *et al.,* 2024, Kanagaraj *et al.,* 2018). Larger particle sizes hinder lithium diffusion pathways due to defects and contaminants, while more significant cell parameters along the b-axis can increase diffusion path length (Amri *et al.,* 2024, Kanagaraj *et al.*, 2018). Within LFP particles, the movement of Li ions can be restricted by these factors, preventing them from hopping to their nearest sites, thereby inhibiting Li ion migration and resulting in poor electronic conductivity and capacity loss (Amri *et al.,* 2024, Kanagaraj *et al.,* 2018).

Excellent high-cycle performance is achieved due to the rapid electron conduction pathway and the energy storage properties provided by the graphene structure. Consequently, the incorporation of graphene significantly enhances the lithium-ion diffusion coefficient by facilitating ion movement within the bulk material (Guan *et al.,* 2019). Graphene exhibits extremely high electron mobility, which can reach up to 250,000 cm^2/Vs at room temperature (Nurazzi *et al.,* 2021). The high charge/discharge performance is likely attributed to the interconnected network of graphene sheets in the macroscopic graphene-based structure, which forms an efficient and continuous electron conductive network to collect or transport electrons to/from the active particles during battery charging and discharging processes (Sun et al., 2021). As a result, LFP/G electrodes exhibit higher rate capacity than LFP electrodes without the addition of graphene. This confirms that the improvement in electrical conductivity of the electrode is due to the addition of graphene as an effective agent/additive (Fu *et al.,* 2019). Hu *et al.* (2013) demonstrated that the highly conductive and homogenously distributed graphene around LFP is key to the enhanced cycling performance, where electron migration throughout the charge/discharge process is facilitated by the fast pathways provided by the homogeneous distribution of graphene (Hu *et al.,* 2013). Essentially, electron transfer in amorphous sp^3 carbon is lower compared to sp^2 carbon, such as graphene. During charge/discharge, electrons can spread uniformly across the surface of LFP/G through the graphene conductive layer, which enhances the reversibility and kinetics of the lithium insertion/extraction cycle. Thus, the dynamic limitations caused by the poor conductivity of LFP have been overcome with the addition of graphene, leading to enhanced electrochemical performance in LFP-based cathode materials (Guan *et al.,* 2019).

3.3 X-ray diffraction (XRD) analysis

Fig. 6 shows the XRD characterization results of commercial LFP, LFP/FLG, and LFP/VFLG samples with 1 wt.% and 4 wt.% graphene content in LFP. It can be observed that the diffraction patterns for each sample, indexed by the Pnma

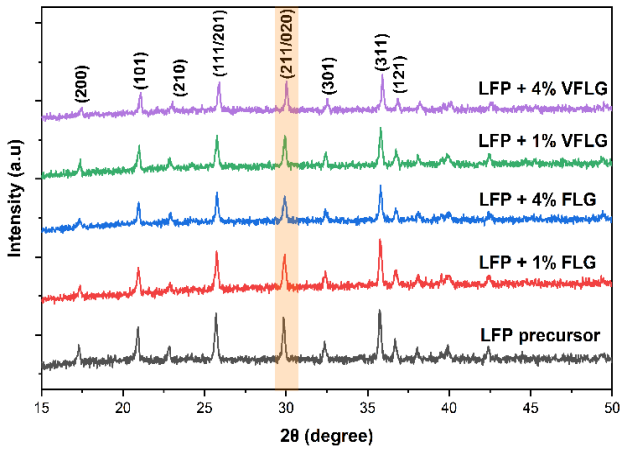

Fig. 6 X-ray diffraction (XRD) analysis of LFP precursor, LFP/G (1 wt.% and 4 wt.% FLG) samples.

orthorhombic phase of LFP (JCPDS 01-083-2092), closely match/almost identical to the olivine structure of LFP. These results indicate that each sample exhibits high purity and crystallinity with a single-phase LFP (Amri *et al.,* 2024). According to Ma *et al.* (2015), good crystallinity of LFP benefits the Li^+ diffusion process and can enhance the electrochemical performance of the material (Ma *et al.,* 2015). Based on the unchanged XRD phase and the known non-reactive nature of graphene under the present processing conditions, the graphene is expected to be mainly physically attached to LFP particles (physisorption/van der Waals contact) (Amri *et al.*, 2024). Li *et al.* (2018) stated that the absence of peaks corresponding to graphene detected in the XRD pattern may be due to the low graphene content (Li *et al.*, 2018).

In Fig. 6, the highest peaks for the active cathode material phase of commercial LFP are observed at 2θ angles of 35.8°, 32.4°, 29.9°, 25.7°, and 20.9°, indexed to the diffraction lines (311), (301), (211/020), (111/201), and (101) corresponding to the pure orthorhombic LFP crystal phase (Pnma) (Table 4) (Mayasari *et al.,* 2023). The high crystallinity of the synthesized material is evident from the sharpness of the peaks, with the stronger peak at 30° (211) indicating particle growth along the ac plane of the orthorhombic LFP crystal (Pnma space group). This phenomenon supports the Li^+ migration along the smaller axis (or b-axis) of the crystal (Mayasari *et al.*, 2023). All LFP samples with FLG and VFLG additions still correspond to the LFP reference with an orthorhombic Pnma crystal structure (JCPDS No. 01-083-2092), as shown in Table 3 (Sofyan *et al.*, 2018). Each LFP/G sample exhibits similar characteristic peaks indexed to the diffraction lines (311), (301), (211/020), (111/201), and (101) of the pure orthorhombic LFP crystal phase, indicating that the LFP crystal structure remains stable. This suggests that the addition of graphene does not alter the primary phase of LFP (Fathollahi *et al.,* 2015).

The lattice parameters and average crystalline size of LFP/VFLG and LFP composites are provided in Table 5. The average crystalline size (D) was determined from the full width at half maximum (FWHM) of the notable diffraction peaks corresponding to Miller indices (020), (111), (101), (301), and (311), using the Scherrer formula as shown in Equation 5 (Chand et al., 2020).

$$\boldsymbol{D = \frac{K\lambda}{\beta\, COS\, \theta}} \qquad (5)$$

Where K is the Scherrer constant (0.9), λ is the wavelength of the X-ray used (Cu, λ = 0.15406 Å), β is the full width at half

Table 4
Comparison of XRD data for LFP, LFP/FLG LFP/VFLG, and standard JCPDS data (pattern No. 01-083-2092).

2θ°	JCP DS	LFP	LFP composites/			
			1 wt.% FLG	4 wt.% FLG	1 wt.% VFLG	4wt.% VFLG
101	20.8	20.9	21.0	21.0	21.0	21.1
111/201	25.6	25.7	25.8	25.8	25.8	25.9
211/020	29.7	29.9	29.9	29.9	29.9	30.1
301	32.2	32.4	32.4	32.4	32.4	32.6
311	35.6	35.8	35.8	35.8	35.8	35.9

Table 5
Lattice parameters and crystallin size of LFP, LFP/FLG, and LFP/VFLG.

Sample (wt.%)	a (Å)	b (Å)	c (Å)	V(Å^3)	Space Group	Crystallin Size, D (nm)
LFP	10.23	5.98	4.67	285.00	Pnma	44.21
LFP + 1% FLG	10.20	5.97	4.66	283.22	Pnma	40.25
LFP + 4% FLG	10.21	5.97	4.65	283.13	Pnma	45.13
LFP + 1% VFLG	10.19	5.96	4.65	282.79	Pnma	43.85
LFP + 4% VFLG	10.15	5.94	4.63	279.24	Pnma	45.64
Standard	10.33	6.01	4.69	291.50	Pnma	-

maximum (FWHM) in radians, and θ is the diffraction angle in radians. As shown in Fig. 6, the peaks for samples with 1 wt.% FLG/VFLG addition are broader than those for samples with 4 wt.% FLG/VFLG, indicating smaller nanoparticles for the 1 wt.% FLG/VFLG composites compared to the 4 wt.% FLG/VFLG composites (Wang *et al.*, 2018). Table 5 presents the lattice parameters and particle sizes for LFP, LFP/FLG, and LFP/VFLG, agreeing with the standard JCPDS data.

In Table 5, LFP/FLG and LFP/VFLG have a smaller unit cell volume compared to LFP, indicating that LFP/FLG and LFP/VFLG crystals exhibit more defects compared to LFP. Previous studies have reported that Fe* impurities and lithium-ion vacancies (LIV) are the causes of imperfections in the olivine structure of LFP. These vacancies lead to a decrease in lattice parameters, such as the unit cell volume of LFP (lattice distortion) and the generation of polaron holes (caused by the change in the valence state of Fe from +2 to +3) (Amri *et al.*, 2024, Wang *et al.*, 2016).

As shown in Table 5, the addition of FLG/VFLG causes slight reductions in the a, b, and c-axis. These findings align with previous research, which reported that the incorporation of graphene to LFP leads to a slight decrease in the a-axis, b-axis, and c-axis, leading to a reduction in unit cell volume (Amri *et al.*, 2024, Tian *et al.,* 2015, Yue *et al.,* 2014). It has been previously stated that lithium-ion intercalation/deintercalation occurs via a zig-zag diffusion pathway confined to the a–b axis (Yue *et al.*, 2014). Therefore, the reduced unit cell volume of LFP/G along the a and b-axis can shorten the lithium-ion diffusion distance, thereby enhancing the lithium-ion transfer coefficient. (Yue *et al.,* 2014). As reported by Tian *et al.* (2015) and Amri *et al.* (2024), Li^+ tend to move more easily in the b-axis direction due to the lowered diffusion energy barrier, making the reduction in the b-axis dimension positively impact the electrochemical performance of LFP cathodes (Amri *et al.,* 2024, Tian *et al.*, 2015). The decreased size along the b-axis direction helps shorten the lithium-ion diffusion path within the crystal lattice, resulting in an increased lithium-ion diffusion rate and improved current-carrying capacity of the material (Tian *et al.,* 2015). Pei *et al.* (2012) state that shortening the lithium-ion diffusion path in the b-axis direction effectively improves the electrochemical characteristics of LFP nanomaterials (Pei *et al.*, 2012). Tian et al (2015) also reported that minor changes in the unit cell size can improve the electrochemical characteristics of the cathode. The crystal structure of LFP after the addition of 4 wt.% VFLG is presented in Fig. 7.

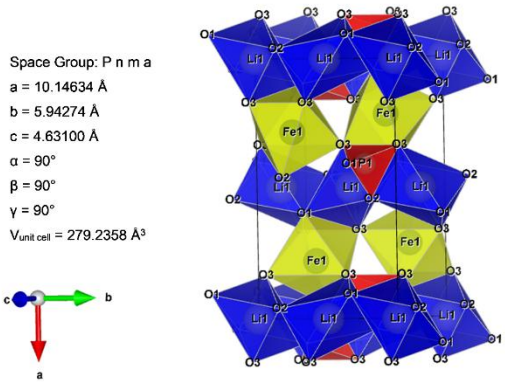

Fig. 7 Crystal structure of LFP + 4 wt.% VFLG.

LFP has an orthorhombic olivine structure (space group: Pnma). The 4C and 4a octahedral sites are filled by iron and lithium atoms, respectively. Phosphorus atoms reside in the tetrahedral sites, while oxygen atoms are positioned in a somewhat distorted and compact hexagonal pattern, giving the material a 3D structure, as shown in Fig. 7 (Rossouw et al., 2017). Changes in the lattice parameters indicate that the addition of graphene to LFP leads to a modest rise in the unit cell volume of LFP/G, as displayed in Table 5. A 3D network is formed by tetrahedral PO_4 with channels traversed by lithium ions along the b- and c-axis. These channels are not interconnected, so the lithium ions within them can hop back and forth between the channels. This suggests that lithium ions travel in a unidirectional manner, and their diffusion will be impeded when blockages occur within these channels (Rossouw et al., 2017).

3.4 Fourier transform infrared spectroscopy (FTIR) analysis

Fig. 8 shows the FTIR characterization results for LFP precursor, LFP/FLG, and LFP/VFLG samples with 1 wt.% and 4 wt.% graphene compositions. Generally, all spectra are spread in two wavelength ranges, namely 400–690 cm^{-1} and 940–1120 cm^{-1}, which align to the internal stretching and bending modes, as well as the external oscillation of the PO_4^{3-} group (Yu *et al.,* 2009). The band observed in the 400–690 cm^{-1} range

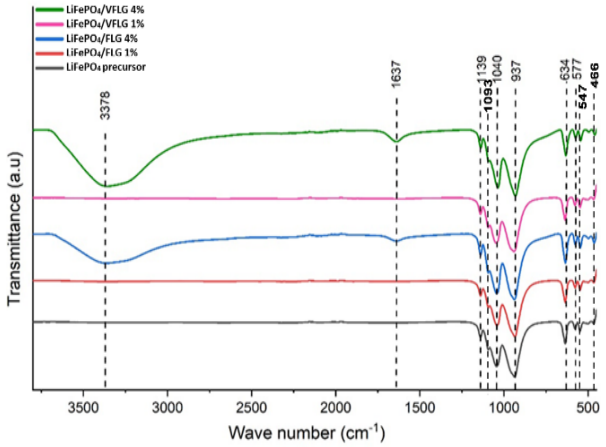

Fig. 8 FTIR spectra of LFP precursor, LFP/G (1 wt.% and 4 wt.%).

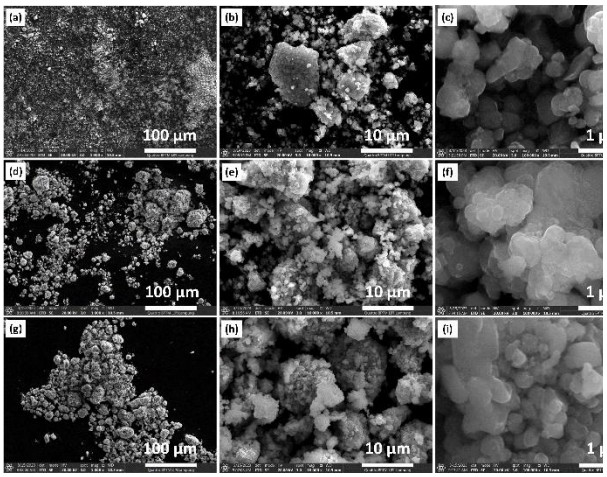

Fig. 9 FESEM analysis of LFP/G (a-c) commercial LFP, (d-f) LFP/4 wt.% FLG, (g-i) LFP/4 wt.% VFLG at magnifications of 1000x, 10,000x, and 100,000x.

corresponds to the v_2 and v_4 vibration modes of the phosphate ion, while the band in the 700–1139 cm^{-1} range corresponds to the internal v_1 and v_3 vibration modes of the phosphate ion within the LFP structure (Bezerra *et al.*, 2021). The absence of peaks in the 700–900 cm^{-1} range indicates the exceptional purity of the synthesized material, as the bands appearing in this spectral range are typical of other phosphate compounds, including $FePO_4$, $P_3O_{10}^{5-}$, and $P_2O_7^{4-}$, which can form as by-products during the fabrication process (Bezerra *et al.,* 2021). The highly delocalized electrons on the graphene plane make it chemically inert. This confirms that the addition of FLG/VFLG does not trigger side reactions during the formation of LFP nor affect the chemical structure of the LFP precursor(Amri *et al.,* 2024).

In Fig. 8, each sample shows the asymmetric stretching vibration v_3 (F_2) of the P–O bond, observed at peaks around ~1040 cm^{-1} and ~1093 cm^{-1} (Amri *et al.,* 2024). The peaks of approximately ~937 cm^{-1} and ~1139 cm^{-1} are ascribed to the symmetric stretching vibration $v_1(A_1)$ of the P–O group in $(PO_4)^{3-}$ (Amri *et al*., 2024). Furthermore, the intramolecular symmetric stretching vibration of the Fe–O bond in the FeO_6 structure is observed at distinct peaks around ~577 cm^{-1} and ~634 cm^{-1} (Amri *et al*., 2024). The peak center of approximately ~547 cm^{-1} is unique to the vibration of lithium ions at the octahedral position of PO_4^{3-}(Amri *et al*., 2024). In contrast, the absorption peak in the range ~466 cm^{-1} relates to the symmetric deformation vibration v_2(E) of the O–P–O group (Amri *et al*., 2024). Additionally, the addition of 4 wt.% FLG and VFLG shows broad absorption peaks at ~3378 cm^{-1} and ~1637 cm^{-1}, associated with water molecules (H_2O), specifically the OH stretching (Amri *et al.,* 2024).

3.5 Field emission scanning electron microscopy with energy dispersive X-ray (FESEM-EDX) analysis

Fig. 9 shows the FESEM characterization results of the LFP precursor, LFP/FLG, and LFP/VFLG samples with 4 wt.% graphene addition. Fig. 9(a_1), 9(b_1), and 9(c_1) depict the particle size distribution of each sample. In Fig. 9(a), the LFP precursor sample exhibits predominantly small particles evenly distributed without significant agglomeration. The LFP composite with FLG addition (Fig. 9(b)) and VFLG addition (Fig. 9(c)) shows a quasi-spherical particle structure. Specifically, the addition of 4 wt.% FLG (Fig. 9(b)) results in moderately well-dispersed and relatively small particles, with some agglomeration leading to larger clusters. Meanwhile, the addition of 4 wt.% VFLG (Fig. 9(c)) demonstrates significant agglomeration of particles into larger clusters. This agglomeration occurs during the mixing and stirring process of LFP with FLG/VFLG. According to Jeon *et al.* (2020), most LFP nanoparticles wrapped in graphene sheets have been observed to connect with other LFP particles (Jeon *et al.,* 2020). This connection facilitates lithium-ion diffusion through nano-porous channels surrounded by graphene, thereby enhancing electronic conductivity (Honggowiranto & Kartini, 2016). The addition of graphene to LFP creates new pathways surrounding the LFP particles (Kucinskis et al., 2013). These interconnected conductive pathways improve electron transport during electrochemical reactions, thereby enhancing the electrochemical properties of the LFP cathode (Fu *et al.,* 2019, Jeon *et al.,* 2020). Compared to the LFP precursor, the addition of graphene has been proven to increase the charge-discharge capacity of the LFP cathode

Fig. 10-11 shows the electron micrographs and elemental mapping results using ESPRIT Compact software for the LFP/4 wt.% FLG (Fig. 10) and LFP/4 wt.% VFLG (Fig. 11) samples. In Fig. 10(a) and Fig. 11(a), it can be observed that the elements carbon (C), oxygen (O), phosphorus (P), and iron (Fe), in the LFP/4 wt.% VFLG sample are more homogeneously distributed compared to the LFP/4 wt.% FLG sample, as indicated by the uniform color in the mapping results. The carbon (C) element is also well distributed across the sample in the 4 wt.% VFLG addition, indicating a homogeneous distribution of graphene. However, lithium (Li) cannot be detected by EDX due to its low atomic weight. Furthermore, the percentages of C, Fe, O, and P

Table 6
Percentage of elements in LFP/4 wt.% FLG/VFLG.

Elements	LFP/4 wt.% FLG		LFP/4 wt.% VFLG	
	Weight percentages (%wt.)	Atomic percentages (at. %)	Weight percentages (%wt.)	Atomic percentages (at. %)
C	8.55	16.33	7.75	14.36
O	39.18	55.18	44.04	61.3
P	18.28	13.51	15.97	11.48
Fe	34.02	13.97	32.24	12.86

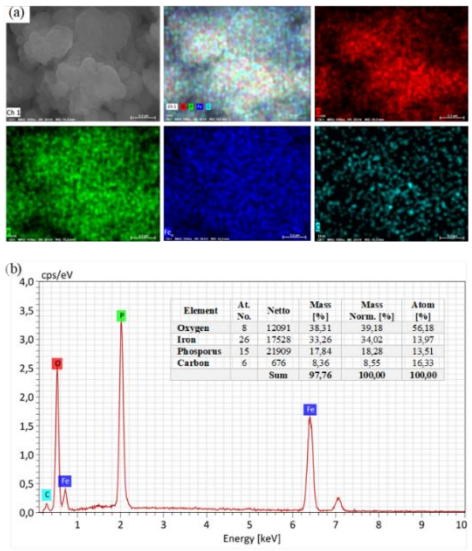

Fig. 10 Electron micrograph and elemental mapping using FESEM-EDX for the LFP/FLG sample with 4 wt.% FLG addition.

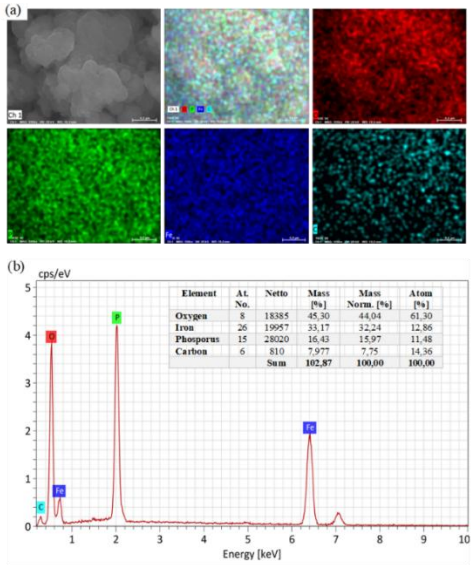

Fig. 11 Electron micrograph and elemental mapping using FESEM-EDX for the LFP/VFLG sample with 4 wt.% VFLG addition.

in the LFP/4 wt.% FLG and LFP/4 wt.% VFLG are revealed in Table 6.

As shown in Table 6, the carbon (C) content in the LFP/4 wt.% FLG sample is slightly higher than in the LFP/4 wt.% VFLG sample. Each graphene layer is composed of carbon atoms arranged in a hexagonal lattice, so the carbon content is directly proportional to the number of graphene layers. FLG, which is dominated by 4-5 graphene layers, has a higher carbon content compared to VFLG, which is dominated by 1-3 graphene layers (Amri *et al.,* 2021). The amount of carbon in LFP can significantly influence the physical and electrochemical properties of the battery. Therefore, the total carbon content must be kept low, as excessive carbon content can degrade the tap density of LFP, potentially affecting the energy and power density of the battery (Chen & Dahn, 2002).

3.6 Electronic properties from DFT computations

We have used the LDA-PWC method (Perdew & Wang, 1992), as implemented in the CASTEP code (Segall *et al.*, 2002), to acquire the density of states (DOS) for the LFP surface. Geometry optimization of the LFP (001) surface and its interface with graphene. Geometry optimization of the LFP(001)/G model revealed only a modest structural relaxation, with an equilibrium interfacial separation of ~2.8 Å. This relatively large spacing suggests that the interaction is dominated by van der Waals forces with limited (partial) charge redistribution across the interface, consistent with a weakly bound heterointerface (Silvestrelli & Ambrosetti, 2015). The optimized structure is illustrated in Fig. 12.

As shown in Fig. 13, pristine LFP exhibits a wide bandgap (~3.7 eV), consistent with its intrinsically low electronic conductivity. The valence band maximum (VBM) is mainly contributed by O 2p states, while the conduction band minimum (CBM) is dominated by Fe 3d states (Zhou *et al.,* 2004). Upon introducing graphene, additional electronic states appear near the Fermi level, primarily arising from the C 2p π orbitals. Consequently, the effective bandgap is reduced to ~1.8–2.0 eV, indicating an increased electronic density of states near the Fermi level and a more favorable electronic transport landscape at the interface. This result supports the interpretation that graphene provides an additional electronic percolation pathway and facilitates charge delocalization at the LFP/G contact through orbital proximity/hybridization between Fe 3d, O 2p, and C 2p states.

The present DFT model represents an idealized basal-plane contact between LFP and a pristine graphene monolayer. In practical high-shear exfoliation, graphene flakes may contain edge-related defects (e.g., vacancies, wrinkles, and grain boundaries) and, depending on processing history, may carry a finite amount of oxygen-containing functional groups (Paton *et al.,* 2014). These realistic features are not explicitly included in the current atomistic model and can modify the electronic properties compared to pristine graphene. For example, edge/vacancy defects may introduce localized states and broaden the DOS near the Fermi level, which can strengthen interfacial electronic coupling, whereas excessive disorder may increase carrier scattering and reduce effective in-plane conductivity (Banhart *et al.,* 2011). Likewise, oxygen functional groups can alter graphene's work function through interfacial dipoles, shifting band alignment and changing the extent and/or direction of charge redistribution (Białoruski *et al.,* 2022, Yan & Chou, 2010). Therefore, the present calculation should be interpreted as a baseline electronic-structure trend, while the absolute magnitude of charge transfer or bandgap modification may differ for defect- or functionalized graphene produced by shear exfoliation.

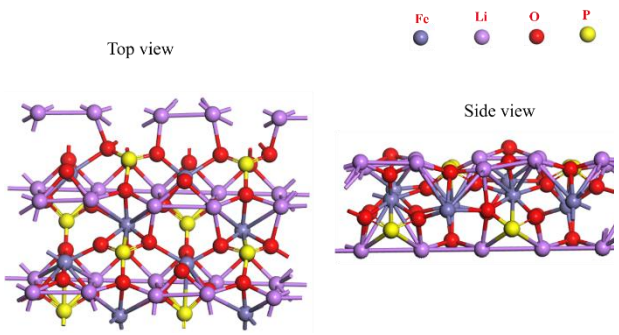

Fig. 12 Optimized structure for the LFP surface.

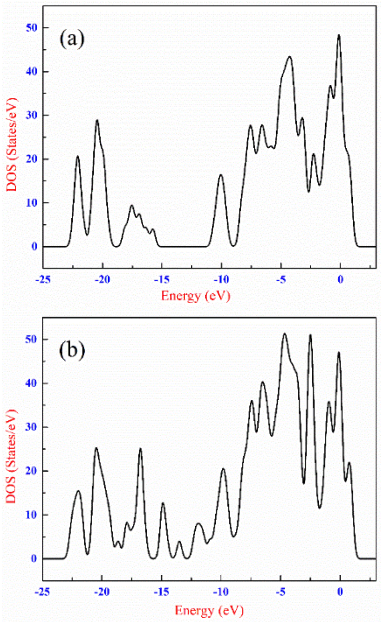

Fig. 13 DOS curves for the LFP surface (a), and the LFP /VFLG surface (b).

The DFT-predicted emergence of carbon-derived states near the Fermi level provides a physically consistent explanation for the experimentally observed reduction in charge-transfer resistance (EIS, Figs. 1–2) in graphene-containing electrodes, supporting graphene's role in improving interfacial electronic connectivity rather than acting as a purely passive conductive diluent. In addition, the EIS-derived transport analysis (Table 2) indicates a reduced Warburg contribution (smaller σ) and a higher apparent diffusion coefficient (D_{Li^+}) for graphene-modified electrodes. It is emphasized that D_{Li^+} derived from EIS is an apparent/chemical diffusion parameter at the porous-electrode scale and reflects coupled ion–electron kinetics and polarization effects rather than a direct solid-state migration barrier. Thus, the improvement in EIS-derived apparent transport is consistent with enhanced electronic pathways at the interface that can alleviate coupled kinetic limitations during operation (Barsoukov & Macdonald, 2005), but it should not be interpreted as a direct DFT-quantified enhancement of intrinsic Li^+ migration.

A schematic diagram illustrating the interfacial band alignment and electron transfer mechanism between LFP and graphene is presented in Fig. 14. The diagram highlights that the wide intrinsic bandgap of LFP (~3.7 eV) is modified in the presence of graphene, whose π-states contribute near the Fermi level and enable an additional electronic pathway for charge delocalization. This interfacial electronic-coupling picture is consistent with the reduced charge-transfer resistance observed experimentally. The Warburg-region changes in EIS (Table 2) are accordingly discussed as an apparent transport improvement that may arise from reduced polarization and improved electronic connectivity, while direct quantification of Li^+ migration at the interface requires dedicated migration-barrier calculations.

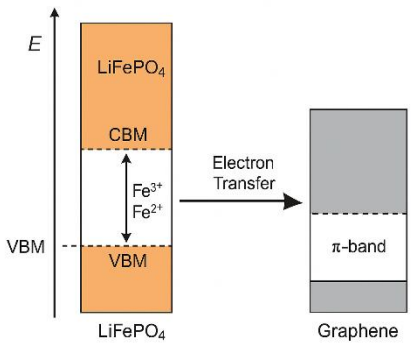

Fig. 14 Schematic band alignment and interfacial electron transfer between LFP and graphene.

4. Conclusion

The performance of $LiFePO_4$ (LFP) cathodes was enhanced by increasing their energy storage capacity through the addition of two types of low-cost graphene with varying FLG (from the TASE process) and VFLG (from the TSSE process) contents ranging from 0 wt.% to 4 wt.%. EIS results indicated that graphene addition promoted improved interfacial electronic connectivity, reflected by a reduced semicircle diameter and lower charge-transfer resistance, particularly for VFLG-containing electrodes. Changes in the low-frequency (Warburg) region suggested an apparent improvement in coupled transport/polarization behavior rather than a direct measurement of intrinsic solid-state Li^+ migration. Galvanostatic charge–discharge tests showed that 4 wt.% FLG and 4 wt.% VFLG delivered the highest specific discharge capacities of 29.98 mAh g^{-1} and 44.66 mAh g^{-1} at 0.5C, corresponding to increases of 81.9% and 170.5% relative to bare LFP. Structural and chemical characterizations (XRD, FTIR) confirmed phase purity and no detectable side reactions upon graphene incorporation, while FESEM/EDX revealed a more homogeneous elemental distribution for LFP/VFLG, consistent with more effective conductive pathways. Maintaining a moderate total carbon level (≈7.8–8.6 wt.%) was advantageous, since excessive carbon could reduce tap density and negatively impact practical energy/power density. DFT calculations on an idealized LFP(001)/graphene interface further supported a qualitative electronic-structure trend, where carbon-derived states near the Fermi level were associated with a reduced effective bandgap relative to pristine LFP, consistent with the experimentally observed decrease in R_{ct} and improved discharge capacity at 0.5C. Finally, comprehensive rate-capability testing up to 5C (including recovery steps) and migration-barrier calculations were recommended as future work to quantitatively assess high-rate performance and interfacial Li^+ transport.

Acknowledgments

This work was supported by Ministry of Higher Education, Science, and Technology Republic of Indonesia via the Fundamental-Reguler research grant (Contract number: 19502/UN19.5.1.3/AL.04/2025).

Author Contributions: A.A.: C conceptualization, funding acquisition, methodology, M., investigation, formal analysis, writing – original draft, A., investigation, formal analysis, writing – original draft, S., project administration, F.M.: supervision, M.A.: writing – review & editing, K.J.: writing – review & editing, M.A.: visualization, C.Y.: resources, S. S.: data curation, M.M.R.: software.

Conflicts of Interest: The authors declare no conflict of interest.

References

Amri, A., Hendri, Y. B., Sunarno, Taer, E., Saputro, S., Pambudi, Y. D. S., & Jiang, Z. T. (2024). Novel LiFePO4/very-few-layer-graphene (LFP/VFLG) composites to improve structural and electrochemical properties of lithium-ion battery cathode. *Ceramics International*, 50(11), 19806–19813. https://doi.org/10.1016/j.ceramint.2024.03.104

Amri, A., Hendri, Y. B., Yin, C. Y., Rahman, M. M., Altarawneh, M., & Jiang, Z. T. (2021). Very-few-layer graphene obtained from facile two-step shear exfoliation in aqueous solution. *Chemical Engineering Science*, 245, 1–13. https://doi.org/10.1016/j.ces.2021.116848

Banhart, F., Kotakoski, J., & Krasheninnikov, A. V. (2011). Structural defects in graphene. *ACS Nano*, *5*(1), 26–41. https://doi.org/10.1021/nn102598m

Barsoukov, E., & Macdonald, J. R. (2005). *Impedance Spectroscopy: Theory, Experiment, and Applications,* (2nd ed.). John Wiley & Sons, Inc.

Bellache, K., Camara, M. B., & Dakyo, B. (2018). Characterization and electric behavior modeling of lithium- battery using temporal approach for parameters computing. *7th International Conference on Renewable Energy Research and Applications (ICRERA)*, 1330–1335. https://doi.org/10.1109/ICRERA.2018.8566742

Bezerra, C. A. G., Davoglio, R. A., Biaggio, S. R., Bocchi, N., & Rocha-Filho, R. C. (2021). High-purity LiFePO4 prepared by a rapid one-step microwave-assisted hydrothermal synthesis. *Journal of Materials Science*, 56(16), 10018–10029. https://doi.org/10.1007/s10853-021-05914-1

Chand, P., Kumar, S., Singh, V., & Singh, N. P. (2020). Investigation of the structural and electrical behavior of LiFePO4 as cathode material for energy storage application. *Materials Today: Proceedings*, 32, 483–486. https://doi.org/10.1016/j.matpr.2020.02.624

Chen, T., Jin, Y., Lv, H., Yang, A., Liu, M., Chen, B., Xie, Y., & Chen, Q. (2020). Applications of lithium-ion batteries in grid-scale energy storage systems. *Transactions of Tianjin University*, 26(3), 208–217. https://doi.org/10.1007/s12209-020-00236-w

Chen, Z., & Dahn, J. R. (2002). Reducing carbon in LiFePO[sub 4]/C composite electrodes to maximize specific energy, volumetric energy, and tap density. *Journal of The Electrochemical Society*, 149(9), A1184. https://doi.org/10.1149/1.1498255

Cruz-Manzo, S., & Greenwood, P. (2020). An impedance model based on a transmission line circuit and a frequency dispersion Warburg component for the study of EIS in Li-ion batteries. *Journal of Electroanalytical Chemistry*, *871*, 114305. https://doi.org/10.1016/j.jelechem.2020.114305

Ding, R., Liu, H., Wang, L., & Liang, G. (2019). Effect of spray drying technological conditions on the performance of LiFePO4/C cathode materials with high energy density. *Ionics*, 25(12), 5633–5642. https://doi.org/10.1007/s11581-019-03162-7

Dixit, A. (2019). Cathode Materials for Lithium Ion Batteries (LIBs): A Review on Materialsrelated aspects towards High Energy Density LIBs. *SMC Bulletin*, 10(3). https://doi.org/https://doi.org/10.48550/arXiv.2008.10896

Eftekhari, A. (2017). LiFePO4/C nanocomposites for lithium-ion batteries. *Journal of Power Sources*, 343, 395–411. https://doi.org/10.1016/j.jpowsour.2017.01.080

Fathollahi, F., Javanbakht, M., Omidvar, H., & Ghaemi, M. (2015). Improved electrochemical properties of LiFePO4/graphene cathode nanocomposite prepared by one-step hydrothermal method. *Journal of Alloys and Compounds*, 627, 146–152. https://doi.org/10.1016/j.jallcom.2014.12.025

Fu, Y., Wei, Q., Zhang, G., Zhong, Y., Moghimian, N., Tong, X., & Sun, S. (2019). LiFePO4-graphene composites as high-performance cathodes for lithium-ion batteries: The impact of size and morphology of graphene. *Materials*, 12(6), 842. https://doi.org/10.3390/ma12060842

Gan, L., Guo, H., Wang, Z., Li, X., Peng, W., Wang, J., Huang, S., & Su, M. (2013). A facile synthesis of graphite/silicon/graphene spherical composite anode for lithium-ion batteries. *Electrochimica Acta*, 104, 117–123. https://doi.org/10.1016/j.electacta.2013.04.083

Gao, L., Ren, W., Li, F., & Cheng, H. M. (2008). Total color difference for rapid and accurate identification of graphene. *ACS Nano*, 2(8), 1625–1633. https://doi.org/10.1021/nn800307s

Gu, Y., & Hu, L. (2021). Effect of graphene addition on microstructure and properties of graphene/copper composite. *IOP Conference Series: Earth and Environmental Science*, 651(3), 032002. https://doi.org/10.1088/1755-1315/651/3/032002

Guan, X., LI, G., LI, C., & REN, R. (2017). Synthesis of porous nano/micro structured LiFePO4/C cathode materials for lithium-ion batteries by spray-drying method. *Transactions of Nonferrous Metals Society of China*, 27(1), 141–147. https://doi.org/10.1016/S1003-6326(17)60016-5

Guan, Y., Shen, J., Wei, X., Zhu, Q., Zheng, X., Zhou, S., & Xu, B. (2019). High-rate performance of a three-dimensional LiFePO4/graphene composite as cathode material for Li-ion batteries. *Applied Surface Science*, 481, 1459–1465. https://doi.org/10.1016/j.apsusc.2019.03.213

Hasanah, L. M., Yudha, C. S., Muzayanha, S. U., Suciutami, D. P., Sari, A. A. N., Inayati, I., & Purwanto, A. (2020). Influence comparison of precursors on LiFePO4/C cathode structure for Lithium ion batteries. *JKPK (Jurnal Kimia Dan Pendidikan Kimia)*, 5(1), 24. https://doi.org/10.20961/jkpk.v5i1.29874

Hassan, N. A. A., & Al-Timimi, M. H. (2025). Influence of Mg incorporation on the structural and electrochemical properties of LiMn1-xMgxO2 cathode material for lithium-ion batteries. *Science and Technology Indonesia*, 10(3), 826–836. https://doi.org/10.26554/sti.2025.10.3.826-836

Honggowiranto, W., & Kartini, E. (2016). Characterization of LiFePO4 cathode by addition of graphene for lithium ion batteries. *AIP Conf. Proc*, 1710, 030045. https://doi.org/10.1063/1.4941511

Hu, L.-H., Wu, F.-Y., Lin, C.-T., Khlobystov, A. N., & Li, L.-J. (2013). Graphene-modified LiFePO4 cathode for lithium ion battery beyond theoretical capacity. *Nature Communications*, 4(1), 1687. https://doi.org/10.1038/ncomms2705

Imteyaz, S., & Rafiuddin. (2023). Doping of Co3O4–ZrO2 in graphene nanoplatelets for enhanced electrochemical catalytic degradation of phenol. *Hybrid Advances*, 4, 100119. https://doi.org/10.1016/j.hybadv.2023.100119

Jayasree, S., Nair, S., & Santhanagopalan, D. (2020). Surface chemical analysis of solid-electrolyte interphase layer on germanium thin films and the effect of vinylene carbonate electrolyte additive. In *Lithium-ion Batteries - Thin Film for Energy Materials and Devices. IntechOpen*. https://doi.org/10.5772/intechopen.90032

Jeon, J.-W., Biswas, M. C., Patton, C. L., & Wujcik, E. K. (2020). Water-processable, sprayable LiFePO4/graphene hybrid cathodes for high-power lithium ion batteries. *Journal of Industrial and Engineering Chemistry*, 84, 72–81. https://doi.org/10.1016/j.jiec.2019.12.022

Kanagaraj, A. B., Al Shibli, H., Alkindi, T. S., Susantyoko, R. A., An, B. H., AlMheiri, S., AlDahmani, S., Fadaq, H., & Choi, D. S. (2018). Hydrothermal synthesis of LiFePO4 micro-particles for fabrication of cathode materials based on LiFePO4/carbon nanotubes nanocomposites for Li-ion batteries. *Ionics*, 24(11), 3685–3690. https://doi.org/10.1007/s11581-018-2662-8

Kucinskis, G., Bajars, G., & Kleperis, J. (2013). Graphene in lithium ion battery cathode materials: A review. *Journal of Power Sources*, 240, 66–79. https://doi.org/10.1016/j.jpowsour.2013.03.160

Li, D., Hou, H., Liu, X., Yao, Y., Dai, Z., & Yu, C. (2018). The synchronous reutilization of the expired ferrous sulfate granules and waste Li foils for LiFePO4/C cathode. *International Journal of Hydrogen Energy*, 43(49), 22419–22426. https://doi.org/10.1016/j.ijhydene.2018.10.105

Li, J., Zhang, L., Zhang, L., Hao, W., Wang, H., Qu, Q., & Zheng, H. (2014). In-situ growth of graphene decorations for high-performance LiFePO4 cathode through solid-state reaction. *Journal of Power Sources*, 249, 311–319. https://doi.org/10.1016/j.jpowsour.2013.10.106

Li, X., Shao, Z., Liu, K., Zhao, Q., Liu, G., & Xu, B. (2018). A facile ultrasound assisted high temperature ball milling synthesis of LiFePO4/graphene with enhanced electrochemical performance. *International Journal of Hydrogen Energy*, 43(41), 18773–18782. https://doi.org/10.1016/j.ijhydene.2018.08.061

Li, Y., Qi, F., Guo, H., Guo, Z., Li, M., & Wu, W. (2019). Characteristic investigation of an electrochemical-thermal coupled model for a LiFePO4/Graphene hybrid cathode lithium-ion battery. *Case Studies in Thermal Engineering*, 13, 100387. https://doi.org/10.1016/j.csite.2018.100387

Liu, T., Sun, S., Zang, Z., Li, X., Sun, X., Cao, F., & Wu, J. (2017). Effects of graphene with different sizes as conductive additives on the electrochemical performance of a LiFePO4 cathode. *RSC Adv.*, 7(34), 20882–20887. https://doi.org/10.1039/C7RA02155K

Ma, H., Xiang, J., & Xia, X. (2018). Graphene foam supported LiFePO4 nanosheets composite as advanced cathode for lithium ion batteries. *Materials Research Bulletin*, 101, 205–209. https://doi.org/10.1016/j.materresbull.2018.01.024

Ma, X., Chen, G., Liu, Q., Zeng, G., & Wu, T. (2015). Synthesis of LiFePO4 graphene nanocomposite and its electrochemical properties as cathode material for Li-ion batteries. *Journal of Nanomaterials*, 2015(1). https://doi.org/10.1155/2015/301731

Mahesh, K. C., Manjunatha, H., Venkatesha, T. V., & Suresh, G. S. (2012). Study of lithium ion intercalation/de-intercalation into LiNi1/3Mn1/3Co1/3O2 in aqueous solution using electrochemical impedance spectroscopy. *Journal of Solid State Electrochemistry*, 16(9), 3011–3025. https://doi.org/10.1007/s10008-012-1739-y

Massé, R. C., Liu, C., Li, Y., Mai, L., & Cao, G. (2017). Energy storage through intercalation reactions: electrodes for rechargeable batteries. *National Science Review*, 4(1), 26–53. https://doi.org/10.1093/nsr/nww093

Mayasari, E., Fukugaichi, S., Johan, E., & Matsue, N. (2023). Low-energy extraction of lignocellulose nanofibers from fresh Musa basjoo pseudo-stem. *Communications in Science and Technology*, 8(2), 108–112. https://doi.org/10.21924/cst.8.2.2023.1211

Mohanty, D., Chang, M.-J., & Hung, I.-M. (2023). The effect of different amounts of conductive carbon material on the electrochemical performance of the LiFePO4 cathode in Li-ion batteries. *Batteries*, 9(10), 515. https://doi.org/10.3390/batteries9100515

Nurazzi, N. M., Abdullah, N., Demon, S. Z. N., Halim, N. A., Azmi, A. F. M., Knight, V. F., & Mohamad, I. S. (2021). The frontiers of functionalized graphene-based nanocomposites as chemical sensors. *Nanotechnology Reviews*, 10(1), 330–369. https://doi.org/10.1515/ntrev-2021-0030

Paton, K. R., Varrla, E., Backes, C., Smith, R. J., Khan, U., O'Neill, A., Boland, C., Lotya, M., Istrate, O. M., King, P., Higgins, T., Barwich, S., May, P., Puczkarski, P., Ahmed, I., Moebius, M., Pettersson, H., Long, E., Coelho, J., … Coleman, J. N. (2014). Scalable production of large quantities of defect-free few-layer graphene by shear exfoliation in liquids. *Nature Materials*, *13*(6), 624–630. https://doi.org/10.1038/nmat3944

Pei, B., Yao, H., Zhang, W., & Yang, Z. (2012). Hydrothermal synthesis of morphology-controlled LiFePO4 cathode material for lithium-ion batteries. *Journal of Power Sources*, 220, 317–323. https://doi.org/10.1016/j.jpowsour.2012.07.128

Perdew, J. P., & Wang, Y. (1992). Accurate and simple analytic representation of the electron-gas correlation energy. *Physical Review B*, 45(23), 13244–13249. https://doi.org/10.1103/PhysRevB.45.13244

Rossouw, C. A., Raju, K., Zheng, H., & Ozoemena, K. I. (2017). Capacity and charge-transport enhancement of LFP/RGO by doping with α-MnO2 in a microwave-assisted synthesis. *Applied Physics A*, 123(12), 769. https://doi.org/10.1007/s00339-017-1355-x

Segall, M. D., Lindan, P. J. D., Probert, M. J., Pickard, C. J., Hasnip, P. J., Clark, S. J., & Payne, M. C. (2002). First-principles simulation: ideas, illustrations and the CASTEP code. *Journal of Physics: Condensed Matter*, 14(11), 2717–2744. https://doi.org/10.1088/0953-8984/14/11/301

Shang, W., Kong, L., & Ji, X. (2014). Synthesis, characterization and electrochemical performances of LiFePO4/graphene cathode material for high power lithium-ion batteries. *Solid State Sciences*, 38, 79–84. https://doi.org/10.1016/j.solidstatesciences.2014.10.002

Silvestrelli, P. L., & Ambrosetti, A. (2015). van der Waals corrected DFT simulation of adsorption processes on transition-metal surfaces: Xe and graphene on Ni(111). *Physical Review B*, *91*(19), 195405. https://doi.org/10.1103/PhysRevB.91.195405

Sofyan, N., Sekaringtyas, P., Zulfia, A., & Subhan, A. (2018). Use of carbon pyrolyzed from rice husk in LiFePO4/V/C composite and its performance for lithium ion battery cathode. *IOP Conference Series: Earth and Environmental Science*, 105, 012023. https://doi.org/10.1088/1755-1315/105/1/012023

Stenina, I., Minakova, P., Kulova, T., & Yaroslavtsev, A. (2022). Electrochemical properties of LiFePO4 cathodes: The effect of carbon additives. *Batteries*, 8(9), 111. https://doi.org/10.3390/batteries8090111

Sun, D., Tan, Z., Tian, X., Ke, F., Wu, Y., & Zhang, J. (2021). Graphene: A promising candidate for charge regulation in high-performance lithium-ion batteries. *Nano Research*, 14(12), 4370–4385. https://doi.org/10.1007/s12274-021-3405-0

Tian, Z., Zhou, Z., Liu, S., Ye, F., & Yao, S. (2015). Enhanced properties of olivine LiFePO4/graphene co-doped with Nb5+ and Ti4+ by a sol–gel method. *Solid State Ionics*, 278, 186–191. https://doi.org/10.1016/j.ssi.2015.06.017

Varrla, E., Paton, K. R., Backes, C., Harvey, A., Smith, R. J., McCauley, J., & Coleman, J. N. (2014). Turbulence-assisted shear exfoliation of graphene using household detergent and a kitchen blender. *Nanoscale*, 6(20), 11810–11819. https://doi.org/10.1039/c4nr03560g

Wang, H., Zhao, N., Shi, C., He, C., Li, J., & Liu, E. (2016). Interface and doping effect on the electrochemical property of graphene/LiFePO4. *The Journal of Physical Chemistry C*, 120(31), 17165–17174. https://doi.org/10.1021/acs.jpcc.6b03449

Wang, L., Zhao, J., He, X., Gao, J., Li, J., Wan, C., & Jiang, C. (2012). Electrochemical Impedance Spectroscopy (EIS) Study of LiNi1/3Co1/3Mn1/3O2 for Li-ion Batteries. *Int. J. Electrochem. Sci.*, *7*, 345–353.

Wang, S., Yi, M., & Shen, Z. (2016). The effect of surfactants and their concentration on the liquid exfoliation of graphene. *RSC Advances*, 6(61), 56705–56710. https://doi.org/10.1039/c6ra10933k

Wang, S., Zhang, J., Gharbi, O., Vivier, V., Gao, M., & Orazem, M. E. (2021). Electrochemical impedance spectroscopy. *Nature Reviews Methods Primers*, 1(1), 41. https://doi.org/10.1038/s43586-021-00039-w

Wang, X., Feng, Z., Huang, J., Deng, W., Li, X., Zhang, H., & Wen, Z. (2018). Graphene-decorated carbon-coated LiFePO4 nanospheres as a high-performance cathode material for lithium-ion batteries. *Carbon*, 127, 149–157. https://doi.org/10.1016/j.carbon.2017.10.101

Wang, Y. (2011). Shorting effects of LiFePO4 cathode in lithium ion batteries. *Journal of New Materials for Electrochemical Systems*, 14(4), 209–212. https://doi.org/10.14447/jnmes.v14i4.91

Yan, J.-A., & Chou, M. Y. (2010). Oxidation functional groups on graphene: Structural and electronic properties. *Physical Review B*, *82*(12), 125403. https://doi.org/10.1103/PhysRevB.82.125403

Yu, F., Zhang, J., Yang, Y., & Song, G. (2009). Reaction mechanism and electrochemical performance of LiFePO4/C cathode materials synthesized by carbothermal method. *Electrochimica Acta*, 54(28), 7389–7395. https://doi.org/10.1016/j.electacta.2009.07.071

Yue, H., Wu, Z., & Li, L. (2014). A novel method for multi-doped LiFePO4/C preparation with phosphating sludge. *Journal of Alloys and Compounds*, 583, 1–6. https://doi.org/10.1016/j.jallcom.2013.08.109

Zhang, Y., Huo, Q., Du, P., Wang, L., Zhang, A., Song, Y., Lv, Y., & Li, G. (2012). Advances in new cathode material LiFePO4 for lithium-ion batteries. *Synthetic Metals*, 162(13–14), 1315–1326. https://doi.org/10.1016/j.synthmet.2012.04.025